Journal of Materials Chemistry A

ROYAL SOCIETY OF CHEMISTRY

PAPER

View Article Online
View Journal

Cite this: DOI: 10.1039/d6ta00784h

Interface-engineered silicon nano-quill electrodes for durable extreme temperature lithium-ion batteries

Janak Basel, †[ab] Morteza Sabet, †*[bc] Peshal Karki, [ab] Mihir Parekh, [ab] Talia M. Sebastian,[d] Yi Ding[d] and Apparao M. Rao *[ab]

Received 27th January 2026
Accepted 8th April 2026

DOI: 10.1039/d6ta00784h

rsc.li/materials-a

Developing thermally stable lithium-ion batteries (LIBs) is essential to enable hybrid and electric vehicles with simplified thermal management and reduced pack weight. Silicon (Si)-based electrodes are widely explored for current LIBs. However, limited attention is given to thermally resilient Si-based electrodes with industry-relevant electrode formulation. Herein, in-house-developed Si nano-quills (SiNQs) were transformed into interface-mediated SiNQ@C-rGO, featuring a nitrogen-doped carbon coating and rGO wrapping, and used to prepare electrodes from aqueous slurries. The electrochemical performance was evaluated using a piperidinium-based ionic liquid electrolyte at 100 °C. The SiNQ@C-rGO electrode delivered 1000 mA h g^{-1} at 840 mA g^{-1} and retained 73% of its capacity after 100 cycles at 420 mA g^{-1}. Conversely, an identical commercial Si nanoparticles (SiNPs)-based electrode displayed poor rate capability and rapid degradation at 100 °C. Additionally, the SiNQ@C-rGO electrode exhibited stable cycling between 50 °C and 100 °C. Post-mortem analyses verified the superior structural stability of the SiNQ@C-rGO electrode, indicating its potential for use in thermally resilient batteries.

Introduction

With global energy demand projected to rise substantially, electrical energy storage (EES) systems that safely and efficiently store and deliver energy are vital.[1,2] Lithium-ion batteries (LIBs) are the most used EES systems in portable electronics and hybrid/electric vehicles. The demand for longer driving range and faster charging is a key factor influencing the adoption of hybrid and electric vehicles. However, operating under these conditions can generate excessive heat within the battery pack. To prevent this, automotive manufacturers employ complex, expensive thermal management systems to maintain LIB cell temperatures below 60 °C, above which rapid degradation and thermal runaway occur.[3–6] Developing battery cells that operate safely and reliably at elevated temperatures (60–100 °C) could simplify battery pack design, thereby significantly reducing both weight and cost.

Traditional liquid LIB electrolytes with organic solvents pose significant safety risks at elevated temperatures. Carbonate solvents, such as ethylene carbonate (EC), are volatile and flammable, thereby limiting battery operation to temperatures below 60 °C.[7,8] Room-temperature ionic liquids (RTILs) offer a viable approach to overcoming this challenge because of their low vapor pressure, wide electrochemical stability window, and structural robustness over a broad temperature range. The use of RTILs to design batteries for operation between 60 °C and 100 °C has been previously investigated.[9–16] Although RTILs are highly viscous and exhibit low to moderate ionic conductivities at room temperature, their ionic conductivity increases substantially at elevated temperatures.[17–22] Because of their thermal stability up to 385 °C and electrochemical stability up to 5.0 V, piperidinium-based RTILs stand out among other investigated RTILs.[21,23–25] High-temperature stability of the electrolyte is also significantly influenced by the choice of Li salts. Commonly used lithium hexafluorophosphate ($LiPF_6$) dissociates into LiF and PF_5 at high temperatures and poses safety hazards,[26] whereas lithium bis(trifluoromethanesulfonyl) imide (LiTFSI, $T_{decomposition}$ ~340 °C)[27] and lithium bis(oxalate) borate (LiBOB, $T_{decomposition}$ ~293 °C)[28] exhibit excellent thermal stability. However, LiTFSI is preferred for elevated temperatures due to its electrochemical stability and lower volatility.[29–31]

Advancing electrodes with high-temperature stability is crucial for realizing safer batteries. Cathodes such as lithium iron phosphate (LFP), lithium nickel manganese cobalt oxide (NMC), and lithium cobalt oxide (LCO) were reported for extreme-temperature batteries (see Table S1). LFP cathodes

[a]Department of Physics and Astronomy, Clemson University, Clemson, SC, 29634, USA. E-mail: arao@clemson.edu

[b]Clemson Nanomaterials Institute, Clemson University, Anderson, SC, 29625, USA. E-mail: ssabet@clemson.edu

[c]Department of Automotive Engineering, Clemson University, Greenville, SC, 29607, USA

[d]US Army DEVCOM GVSC, Warren, MI, 48397, USA

† Author contributed equally to this work.

exhibit a thermal runaway onset temperature (T_{onset}) of ~270 °C, maintaining structural integrity and showing minimal capacity loss at 100 °C.[32–38] NMC cathode with a lower T_{onset} at ~210 °C exhibits accelerated degradation and an increased risk of oxygen release at 100 °C.[38–41] LCO cathodes are less thermally stable at ≥100 °C, with rapid capacity degradation and a potential for thermal runaway risk.[42–44] Therefore, LFP stands out as the safest and most stable cathode up to 100 °C.

Anodes such as graphite and lithium titanate (LTO) were investigated for high-temperature batteries (Table S1), but several challenges limit their performance. In graphite-based anodes, the solid-electrolyte interphase (SEI) decomposition, Li leaching, and flammable gas release can trigger hazardous conditions at ≥100 °C.[39,42,45] Similarly, LTO anodes experience material degradation, gas evolution, and parasitic reactions under extreme temperatures.[41,46–49] Lithium metal anodes were also explored at or above 100 °C; however, issues such as dendrite growth, SEI instability, significant volume fluctuations, and the potential for thermal runaway persist and must be addressed.[35,36,43,44,50] Silicon (Si) has been the focus of extensive research for LIB anodes due to its abundance on Earth, its low-voltage plateau, and high theoretical capacity (3580 mA h g^{-1} at room temperature).[51–53] At elevated temperatures, the issues related to excessive volume expansion of Si, unstable SEI, and side reactions are exacerbated.[6] Hence, effective strategies must be implemented for utilizing Si-based electrodes in high-temperature LIBs. For temperature range of 50 to 90 °C, reported approaches include: (i) incorporating electrolyte additives, such as fluoroethylene carbonate (FEC), to stabilize the SEI layer, (ii) employing structural engineering of Si, such as forming Si-based composites, applying single- or multilayer coatings, and tuning Si morphology, to accommodate volume changes and enhance mechanical integrity, (iii) implementing conditioning techniques to optimize interfacial chemistry and electrode stability, and (iv) utilizing gel or *in situ* formed electrolytes.[54–58] Limited research has been conducted to evaluate the electrochemical performance of Si-based anodes at ≥100 °C. The existing literature primarily focuses on vapor-assisted deposition of Si on three-dimensional current collectors, resulting in relatively low Si mass loading.[21] Hence, there is a need to advance Si-based electrodes that address existing technological gaps by incorporating (i) effective interface engineering, (ii) relatively high Si loading, and (iii) compatibility with industry-relevant electrode formulations utilizing metal foil current collectors.

In this work, Si-containing electrodes on copper foil were fabricated using a water-based slurry formulation with a Si mass loading of 0.8–0.9 mg cm^{-2}. In-house developed Si nano-quills (SiNQs)[59] were used as the active material. Commercial Si nanoparticles (SiNPs, 100 nm diameter) were also used as a baseline for comparison. Prior to electrode preparation, these active materials were transformed into micron-sized SiNQ@C-rGO and SiNP@C-rGO products with dual-carbon protection,[60] wherein SiNQs or SiNPs are conformally coated with a nitrogen-doped carbon layer and anchored to a reduced graphene oxide (rGO) sheet. To evaluate electrodes' electrochemical behavior at 100 °C, an electrolyte with LiTFSI salt and a piperidinium-based RTIL (without organic solvents) was used. At 100 °C, the SiNQ@C-rGO electrode achieved a high reversible capacity of 1259 mA h g^{-1} (1.13 mA h cm^{-2}) at 420 mA g^{-1} and outstanding capacity retention of 73% after 100 cycles. However, the SiNP@C-rGO electrode exhibited a poor cycling performance and rapid capacity decay. The degradation behavior of electrodes was explored in detail through in-depth electrochemical analysis and post-mortem microstructural studies.

Experimental

Materials and chemicals

Graphene oxide (Industrial grade, multilayer, 20 μm particle size, <5 nm thickness, >99% purity) was acquired from MSE Supplies LLC (Tucson, AZ, USA). Commercial SiNPs (spherical, average diameter of 100 nm, >97% purity), carbon black (SuperP), Li chip (99.9% purity, 16 mm diameter, and 0.6 mm thickness), and copper foil (thickness of 10 μm, ≥99.8% purity) were obtained from MTI Corporation (Richmond, CA, USA). Sodium alginate (medium viscosity, CAS number 9005-38-3), dopamine hydrochloride (99% purity), absolute ethanol (200 proof, CAS number 64-17-5), and Tris–HCl buffer solution (10 mM, pH 8.5) were purchased from Fisher Scientific Chemicals (Atlanta, GA, USA). 1-Methyl-1-propylpiperidinium bis(trifluoromethylsulfonyl)imide ($Pip_{13}TFSI$, CAS number 608140-12-1, ≥99%, $H_2O \leq 500$ ppm) ionic liquid, and bis(trifluoromethane)sulfonimide lithium salt (LiTFSI, CAS number 90076-65-6, 99.95% trace metals basis) were acquired from Sigma Aldrich (St Louis, MO, USA).

Preparation of SiNP@C-rGO and SiNQ@C-rGO composite materials

SiNQs were prepared through a templated-assisted sol–gel process and calcination, followed by thermoreduction in a graphite crucible, as described in our prior work.[59] To obtain polydopamine (PDA) coating, 500 mg of Si-based nanoparticles (either SiNQs or commercial SiNPs) were dispersed in 800 mL of Tris–buffer solution using a homogenizer for 15 minutes. Subsequently, the dispersion was mixed with 500 mg of dopamine hydrochloride and stirred using a magnetic stirrer for 24 hours at room temperature. The resulting SiNQ@PDA or SiNP@PDA particles were collected *via* centrifugation at 7000 rpm, washed three times using a water/ethanol (50 : 50 v/v) solution, and subsequently dried using a freeze dryer (at −84 °C at 0.01 mbar) for 3 days. The PDA-coated particles and as-received GO powder were separately dispersed in deionized water using a homogenizer at 200 rpm for 15 minutes each. The mass ratio of SiNQ@PDA (or SiNP@PDA) to GO was 2 : 1. Subsequently, the two dispersions were combined and homogenized for an additional 15 minutes to achieve a uniform dispersion. The resulting mixture was rapidly frozen in liquid nitrogen and subjected to freeze–drying. The material was then heated at 80 °C for 12 hours to obtain the SiNQ@PDA-GO (or SiNP@PDA-GO) material, which was subsequently annealed under argon-hydrogen mixed gas (9 : 1 volume ratio) at 200

sccm for 2 hours at 700 °C, with a 2 °C min^{-1} heating rate to create the SiNQ@C-rGO (or SiNP@C-rGO) structure.

Preparation and testing of half-cells

The slurry for the electrodes was prepared by mixing SiNQ@C-rGO (or SiNP@C-rGO) powder, Super P conductive additive, and sodium alginate binder in a weight ratio of 8 : 1 : 1 in deionized water. The aqueous mixture was well-mixed overnight using a magnetic stirrer. The slurry was coated onto copper foil using a doctor blade (MTI Corporation) and left to dry overnight in a vacuum oven (MTI Corporation) at 80 °C. The CR2032-type coin cells were crimped inside an argon-filled Vigor glove box (H_2O and O_2 content <0.1 ppm) using the electrode punchout of 12 mm diameter. SiNQ (or SiNP) mass loading in the electrodes used in this work was maintained at ~0.8–0.9 mg cm^{-2}. A Li chip counter electrode, Celgard 2325 separator, and ionic liquid electrolyte (0.8 M LiTFSI in $Pip_{13}TFSI$) were used. After assembly, the half-cells were connected to cell holders within a Neware environmental chamber and tested over a temperature range of 25 °C to 100 °C. The temperature was increased at a ramp rate of 1 °C min^{-1}. Prior to electrochemical testing, the half-cells were held at the target temperature for 10 hours.

Galvanostatic (dis)charging was conducted between 0.01 and 1.0 V using a Neware battery testing system. The cell temperature was maintained at a set temperature throughout the testing period. Each cell was subjected to a formation cycle at a current of 210 mA g^{-1}, followed by cycling at the required currents. The EIS measurements were conducted on SiNQ@C-rGO and SiNP@C-rGO half cells in the frequency range of 100 kHz to 0.1 Hz, with a small AC signal amplitude of 10 mV. All EIS measurements were performed in the fully lithiated state (*i.e.*, 0.01 V *vs.* Li/Li^+) after the 1st, 10th, 50th, and 100th cycles using a Gamry Interface 1010E potentiostat.

Characterizations

A Hitachi Regulus 8230 high-resolution scanning electron microscope (SEM) was used for microstructural studies of powders and electrodes. Dimensional quantization of the particles in SEM images was performed using ImageJ software. Scanning transmission electron microscopy (S-TEM) tests were performed on composite particles using a Hitachi SU9000 ultra-high-resolution SEM operating at 30 kV, loaded with energy-dispersive X-ray spectroscopy (EDS). The X-ray diffraction (XRD) measurements on powders were performed using a Rigaku SmartLab X-ray diffractometer. Raman spectroscopy was conducted using a Renishaw inVia Raman microscope, equipped with a 532 nm laser and a 10× objective lens. Thermogravimetric analysis (TGA) was performed under air (25 mL min^{-1}) from room temperature to 700 °C at a heating rate of 5 °C min^{-1} using a Q5000 thermal analyzer (TA Instruments). The specific surface area and total pore volume of pristine SiNQs and SiNPs were determined using a Quantachrome Autosorb iQ gas sorption analyzer with nitrogen gas.

Results and discussion

Both SiNQ@C-rGO and SiNP@C-rGO products were synthesized following the procedure described in our previous work.[60] In brief, SiNQs (or SiNPs) were conformally coated with polydopamine (PDA) and uniformly dispersed with graphene oxide (GO) in deionized water, followed by rapid freezing, freeze–drying, and subsequent annealing under argon/hydrogen atmosphere. The microstructure of SiNP@C-rGO was detailed in an earlier study.[60] The morphology of a PDA-coated SiNQ (SiNQ@PDA) particle, along with the corresponding elemental maps of Si, carbon (C), oxygen (O), and nitrogen (N), is shown in Fig. 1a and b. The Si and O maps connote the presence of silicon suboxide in SiNQs, consistent with SiNQ's preparation *via* the thermoreduction of silica nano-quills.[59] A uniform N-doped C layer, originating from PDA, encapsulates the SiNQ particle (Fig. 1b). A representative S-TEM image of SiNQ@C-rGO (Fig. 1c) shows a micron-sized composite particle with the presence of an rGO sheet. The corresponding Si and O maps (Fig. 1d) indicate a uniform distribution of SiNQs across the rGO surface, which is further verified by SEM images (yellow arrows in Fig. 1e). Fig. S1 presents a zoomed-in view of several SiNQs within the SiNQ@C-rGO composite shown in Fig. 1c. Yellow arrows mark tubular SiNQ particles. The C map reveals a thin C coating on SiNQ particles as well as their wrapping by an rGO sheet. In addition, the N map clearly shows nitrogen doping within the SiNQ@C particles. The dual carbon coating of active particles is expected to buffer volume fluctuations during cycling at 100 °C.

The XRD and Raman spectroscopy results for SiNP, SiNQ, SiNP@C-rGO, and SiNQ@C-rGO are presented in Fig. 2. The XRD patterns of all four materials (Fig. 2a) show the characteristic diffraction peaks of crystalline Si. In addition, a broad and weak peak centered at around 23° is observed for SiNQ and SiNQ@C-rGO, corresponding to amorphous silicon suboxide (SiO_x).[59] Both SiNP@C-rGO and SiNQ@C-rGO exhibit additional peaks associated with hexagonal graphitic structure (PDF card no. 00-041-1487),[61] including a prominent graphitic C(002) peak at 26.38°, along with smaller peaks near 44° and 54°. These features originate from the dual carbon framework. The Raman spectra of all materials (Fig. 2b) display the characteristic crystalline Si peak at ~520 cm^{-1} and a broader band near 920 cm^{-1}.[62] As expected, the Si peaks in SiNQ and SiNQ@C-rGO are broader than those in SiNP@C-rGO, reflecting the presence of silicon suboxides.[59] Carbonaceous protective layers in SiNP@C-rGO and SiNQ@C-rGO give rise to two peaks at 1350 and 1590 cm^{-1}, corresponding to the D-band (disordered carbon) and G-band (sp^2-hybridized carbon), respectively.[60] The presence of rGO is known to enhance both electronic conductivity and Li-ion diffusivity.[63,64]

The SiNQ and SiNP contents in composite materials were quantified by TGA conducted in air. The resulting thermograms and corresponding derivative weight profiles are shown in Fig. 2c and d. Both SiNQ@C-rGO and SiNP@C-rGO exhibit a two-step weight loss between 350 and 650 °C, attributed to the sequential oxidation of amorphous carbon and rGO. In the

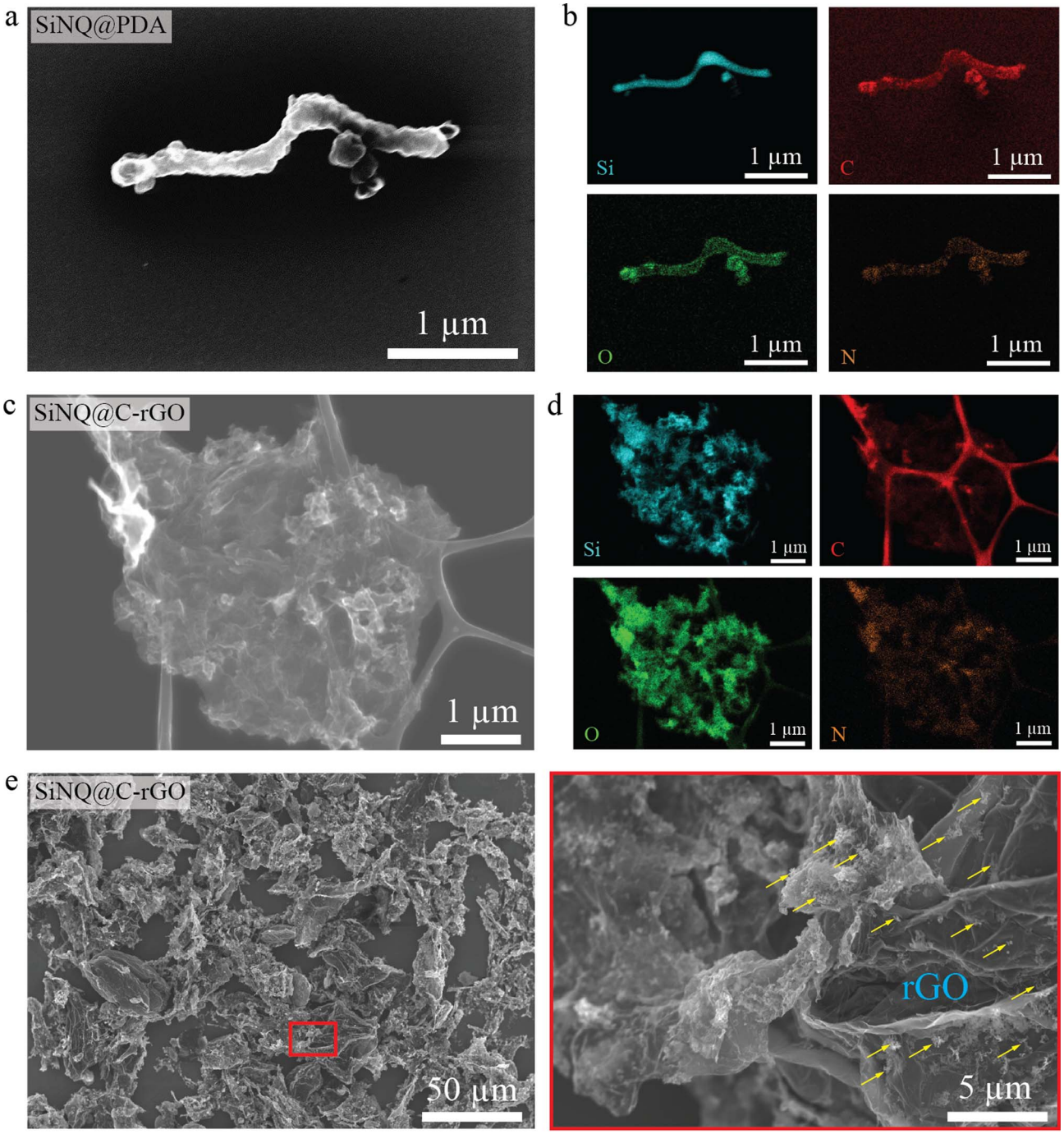

Fig. 1 (a) S-TEM image and (b) the corresponding elemental maps of a SiNQ@PDA intermediate particle, (c) S-TEM image, and (d) the corresponding elemental maps of the final SiNQ@C-rGO composite particle with a dual carbon protection technology, and (e) SEM micrographs of SiNQ@C-rGO product, confirming distribution of SiNQ@C particles (marked by yellow arrows) over the surface of a rGO sheet.

derivative weight profile of SiNP@C-rGO, two distinct peaks are observed, whereas for SiNQ@C-rGO, the first peak partially overlaps with the second peak, appearing as a shoulder. This difference is attributed to the morphologies of pristine SiNPs and SiNQs. As summarized in Table S2, SiNQs possess a significantly higher surface area and pore volume than SiNPs. With a similar amount of PDA, the resulting carbon coating on SiNQs is therefore expected to be thinner than that on SiNPs. This results in a shorter thermal degradation step for SiNQ@C-rGO, characterized by a shoulder. After completing thermal degradation of carbons, both thermograms reach a minimum (inset, Fig. 2c), followed by a gradual mass increase due to the oxidation of SiNQs or SiNPs. The minimum points in the thermograms indicate the estimated contents of SiNQ (~76.0 wt%) and SiNP (~61.5 wt%) in the composite materials. It is observed that the SiNP@C-rGO composite exhibits significantly lower

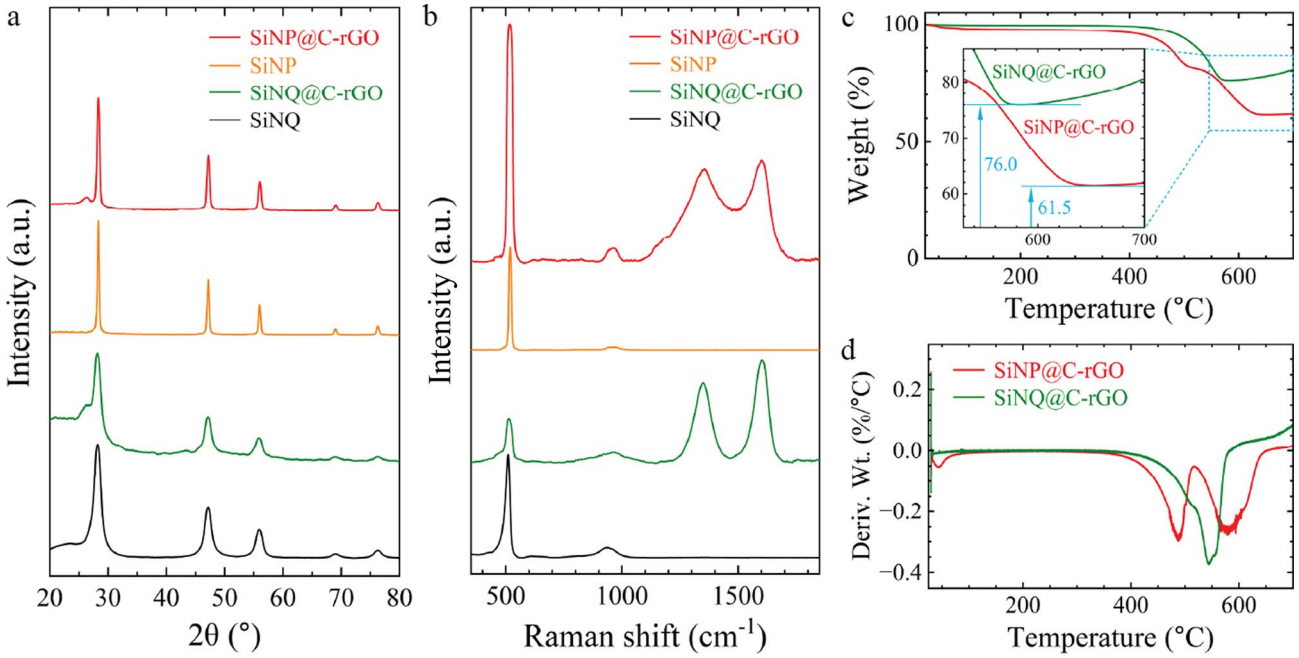

Fig. 2 (a) XRD patterns and (b) Raman spectra of pristine SiNPs, SiNQs, SiNP@C-rGO, and SiNQ@C-rGO. (c) TGA thermograms and (d) their corresponding derivative weight curves for SiNP@C-rGO and SiNQ@C-rGO. TGA tests were conducted in air to oxidize all carbonaceous materials.

specific surface area and pore volume than pristine SiNPs, whereas dual carbon coating of SiNQs increases the specific surface area and pore volume (see Table S2). The formation of a thick PDA-derived carbon layer on solid SiNPs appears to block available interparticle pores, resulting in a marked decrease in both total pore volume (from 0.12 to 0.05 $cm^3\ g^{-1}$) and specific surface area (from 56.2 to 23.0 $m^2\ g^{-1}$). In contrast, applying a thin conformal carbon coating to highly porous SiNQs slightly increases the total pore volume (from 0.64 to 0.88 $cm^3\ g^{-1}$) and enhances the available surface area (from 399.5 to 488.0 $m^2\ g^{-1}$), suggesting that the porosity of SiNQs is preserved after composite formation.

The SiNQ@C-rGO and SiNP@C-rGO composites were employed to fabricate robust electrodes using water-based slurries. The SEM micrographs of electrodes (Fig. S2) indicate a uniform distribution of composite particles over the surface and cross-section of the electrode coating. Half-cells were prepared using these electrodes, and their electrochemical performances at 100 °C are presented in Fig. 3. The charge–discharge profiles of both cells at currents of 210, 420, and 840 mA g^{-1} are shown in Fig. 3a. At the low current of 210 mA g^{-1}, the SiNP@C-rGO cell delivers a higher reversible capacity, but undergoes a sharp capacity decline at higher currents. In contrast, the SiNQ@C-rGO cell exhibits a more gradual capacity decay with increasing the applied current. With increasing current, the SiNP@C-rGO cell exhibits a leftward shift in the discharge plateau onset, suggesting a pronounced reduction in capacitive contributions at higher currents. Conversely, the nearly unchanged discharge plateau onset of SiNQ@C-rGO indicates minimal variation in capacitive behavior, implying improved charge transport and structural robustness under high-rate operation. Since both half-cells use the same electrolyte, this contrasting behavior can be attributed to the structural integrity and high porosity of SiNQ@C-rGO, which facilitates ion diffusion and buffers mechanical stresses.

The rate capability results (Fig. 3b) further support this observation. At 210 mA g^{-1}, the SiNP@C-rGO cell exhibits a higher initial capacity of 2700 mA h g^{-1} compared to 1600 mA h g^{-1} for the SiNQ@C-rGO cell. However, upon cycling at higher currents, the SiNP@C-rGO cell experiences severe capacity fading, retaining only ~300 mA h g^{-1} at 840 mA g^{-1}. In contrast, the SiNQ@C-rGO cell maintains a significantly higher capacity of ~1000 mA h g^{-1} at the same current, demonstrating the superior rate capability and structural resilience of the SiNQ@C-rGO electrode for fast-charging applications under elevated-temperature conditions.

The cycling stability of both half-cells was evaluated at a current of 420 mA g^{-1} and 100 °C (Fig. 3c). The SiNP@C-rGO and SiNQ@C-rGO cells initially delivered reversible capacities of 2607 and 1260 mA h g^{-1}, respectively. After 10 cycles, the SiNQ@C-rGO cell slightly outperformed SiNP@C-rGO (1210 *vs.* 1198 mA h g^{-1}). Remarkably, after 100 cycles at 100 °C, the SiNQ@C-rGO cell retained a capacity of 924 mA h g^{-1}, corresponding to an outstanding 73% capacity retention. A survey of the literature on Si-based electrodes tested at 100 °C or higher (Table S1) indicates that the SiNQ@C-rGO electrode uniquely integrates several advantages desirable for high-temperature battery applications. These include (i) a relatively high Si mass loading of 0.8–0.9 mg cm^{-2}, (ii) an industry-relevant electrode fabrication process using an aqueous slurry and copper foil, (iii) robust cycling stability with 73% capacity retention after 100

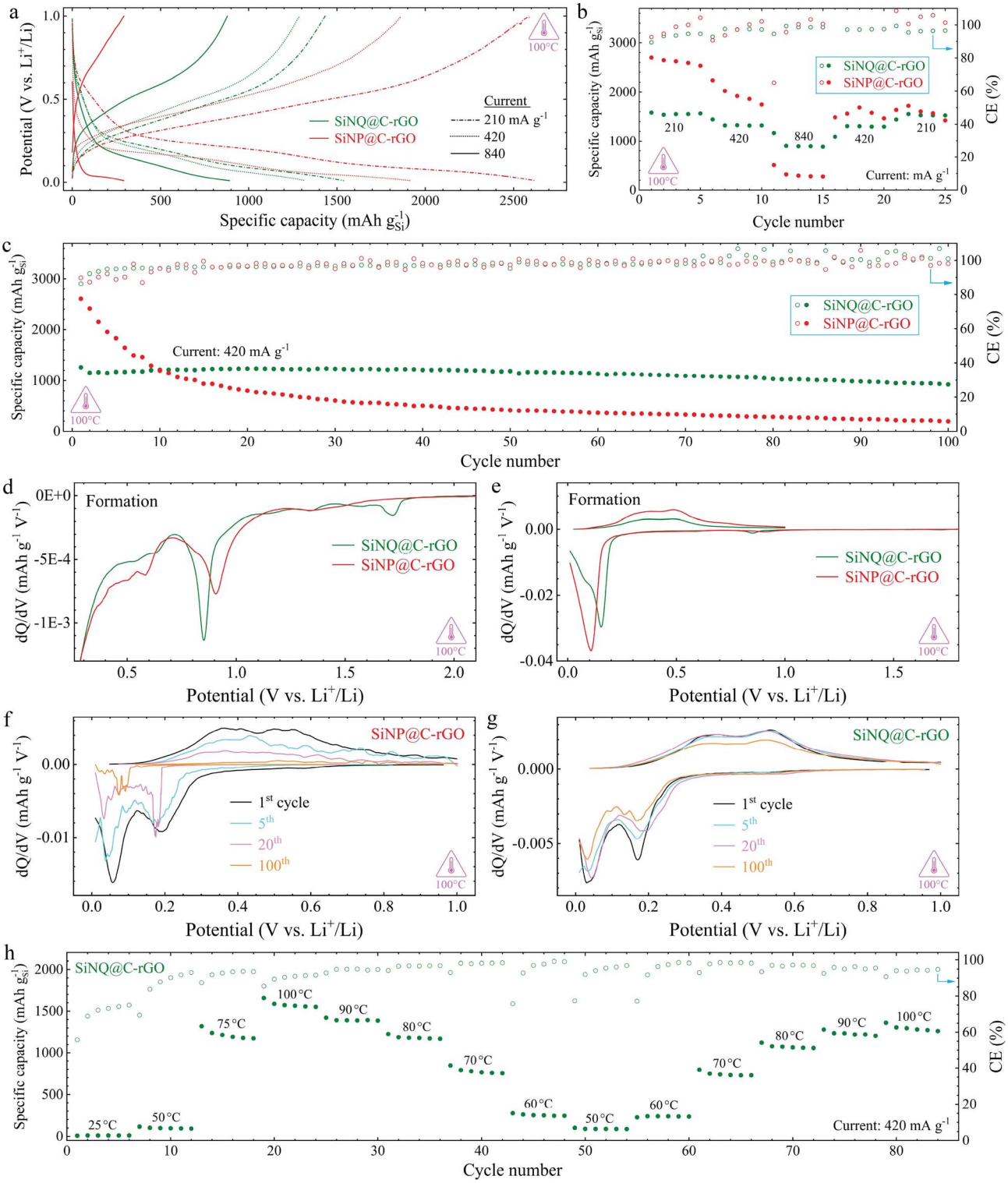

Fig. 3 Electrochemical performance of SiNP@C-rGO and SiNQ@C-rGO half-cells: (a) charge–discharge profiles of the cells at 100 °C at different currents, (b) rate capability of the cells at 100 °C, (c) cycling stability of the cells at 100 °C at a current of 420 mA g^{-1} (d and e) differential capacity curves corresponding to the formation cycle, and (f and g) differential capacity curves related to selected cycles. (h) Cycling performance of a fresh SiNQ@C-rGO half-cell over a temperature range of 25 °C to 100 °C at a current of 420 mA g^{-1}. This electrode retained its capacity during thermal cycling, although some capacity reduction was observed at temperatures above 90 °C, as expected given the large number (>70) of cycles. Thermal cycling between 100 °C and 50 °C demonstrates the cell's ability to retain capacity, indicating its thermal resilience across a range of temperatures.

cycles at 420 mA g^{-1}, and (v) a high rate capability, delivering ~1000 mA h g^{-1} (equivalent to 0.9 mA h cm^{-2}) at 840 mA g^{-1}.

The engineered dual carbon coating on SiNP@C-rGO and SiNQ@C-rGO electrodes promotes self-healing in response to stress-induced pulverization.[60] Unlike SiNPs, pulverization of SiNQs is expected to be minimal. As shown in our prior work,[59] SiNQs exhibit robust cycling behavior due to their inherently porous tubular structure and the presence of a SiO_x matrix, which together buffer volume variations. Furthermore, the high porosity of SiNQs enables superior performance at high current densities. Through both modeling and experiments, it was demonstrated that SiNQs carry most of the current at higher C-rates in SiNQ–graphite composite electrodes,[59] indicating that a high surface area promotes faster (de)lithiation reactions. Cycling SiNQ@C-rGO electrodes at elevated temperatures is associated with faster (de)lithiation reactions. Under these conditions, the high porosity of SiNQ@C-rGO (Table S2) is expected to contribute to the improved electrode performance. Additionally, Si oxides are known to exhibit greater thermal stability than elemental Si.[65,66] The presence of SiO_x matrix in SiNQs[59] is therefore expected to provide enhanced thermal stability during extreme-temperature cycling at 100 °C.

To elucidate the underlying reasons for the superior performance of SiNQ@C-rGO, differential capacity (dQ/dV) plots are presented in Fig. 3d–g. A small SEI formation peak observed at ~1.7 V for the SiNQ@C-rGO electrode (Fig. 3d) is attributed to the presence of amorphous SiO_x. Although SiNPs have a thin native oxide layer, this formation peak is absent for the SiNP@C-rGO electrode. Both electrodes exhibit a major SEI peak in the 0.85–0.95 V range, corresponding to electrolyte decomposition and subsequent reactions with the electrode surface. The sharper SEI peak observed for SiNQ@C-rGO corresponds to the high surface area of SiNQs (Table S2). Additionally, minor SEI peaks appear at ~0.5–0.6 V for both electrodes. The lithiation process of SiNQ@C-rGO and SiNP@C-rGO (related to Li uptake by both Si/SiO_x and carbon species) occurs between 0.1 and 0.2 V, as indicated by a deep reduction peak in Fig. 3e. During the initial charge, both electrodes exhibit a two-step delithiation behavior within the 0.3–0.5 V range, associated with lithium extraction from both Si and carbon domains. The initial coulombic efficiencies (ICEs) for SiNQ@C-rGO and SiNP@C-rGO cells were determined to be ~35% and ~55%, respectively (data not shown). The lower ICE observed for SiNQ@C-rGO can be attributed to (i) irreversible Li^+ interactions with oxygen in the SiO_x matrix (to form Li_2O and Li_xSiO_y)[67,68] and (ii) the higher surface area of SiNQs (Table S2), which leads to more extensive SEI formation. Fig. 3f shows that as cycling progresses, the dQ/dV curves of SiNP@C-rGO display a pronounced decrease in peak intensities, along with a noticeable increase in curve roughness. This roughening reflects differences in fracture-driven local porosity, tortuosity, and resistance between SiNP and SEI. In contrast, the dQ/dV curves for structurally stable SiNQ@C-rGO (Fig. 3g) retain their shape, position, and peak intensities far more consistently over cycling. The oxide phases produced during the initial lithiation of SiNQs, together with a uniform and robust SEI, ensure SiNQ@C-rGO's enhanced cycling stability at 100 °C.

Electrochemical stability of SiNQ@C-rGO electrodes was assessed over a temperature window from 25 °C to 100 °C (Fig. 3h). Initially, a fresh SiNQ@C-rGO half-cell was cycled at 25, 50, 75, and 100 °C at a current of 420 mA g^{-1}. It is noted that at each temperature, the cell was first cycled at 210 mA g^{-1} to allow SEI formation, followed by cycling at 420 mA g^{-1}. As shown in Fig. 3h, the cell delivers negligible capacity at 25 and 50 °C, likely due to the relatively high viscosity of the IL electrolyte. Cycling at higher temperatures yields average reversible capacities of 1210 mA h g^{-1} at 75 °C and 1570 mA h g^{-1} at 100 °C. Interestingly, the capacity achieved at 100 °C through this stepwise temperature increase exceeds that obtained when a fresh half-cell is directly tested at 100 °C (see Fig. 3c). This gradual temperature increase may promote the formation of a more robust SEI, thereby enhancing capacity at 100 °C. The half-cell was then subjected to a thermal cycle in which the temperature decreased from 100 °C to 50 °C and then returned to 100 °C. The SiNQ@C-rGO electrode retained its capacity during this thermal cycling, although some capacity reduction was observed as the temperature increased to 90 °C and above, as expected given the large number (>70) of cycles.

Electrochemical impedance spectroscopy (EIS) was performed on both SiNP@C-rGO and SiNQ@C-rGO cells at 100 °C (Fig. 4a and c). Variations in series resistance (R_S), SEI resistance (R_{SEI}), and charge-transfer resistance (R_{CT}) are illustrated in Fig. 4b and d. For the SiNQ@C-rGO cell, the R_S, R_{SEI}, and R_{CT} remain relatively unchanged over 100 cycles. A relatively slight increase in R_S after 50 cycles may be attributed to SEI rupture and reformation of a new SEI layer after the 50th cycle onwards. The variations in charge and discharge capacity of the cells during cycling are presented in Fig. S3a and b, and a detailed explanation is provided in the SI. A large increase in R_{CT} for the SiNP@C-rGO cell (see Fig. 4d) indicates SiNP pulverization. However, the R_S decreases slightly with cycling due to the formation of new surfaces, thereby lowering electronic resistance. This compensates for the increased tortuosity caused by pulverization and SEI rupture, further enhancing capacitive impedance and ionic migration resistance. On the other hand, the decrease in capacitive impedance over cycling for the SiNQ@C-rGO cell (*cf.* Fig. 4a), despite constant SEI pulverization, may be explained by the fact that while SEI pulverizes, SiNQ preserves its morphology over cycling,[59] and thinner, porous, freshly formed SEI (after pulverization) facilitates easier electrolyte access.

Post-mortem microstructural studies were conducted. The SiNP@C-rGO electrode (after the formation cycle) and the SiNQ@C-rGO electrode (after 100 cycles) were retrieved, and digital images of the electrodes and separators are presented in Fig. 4e and f. The SiNP@C-rGO electrode appears to be severely pulverized even after formation, with a significant portion of the electrode coating adhering to the separator. In contrast, the cycled SiNQ@C-rGO electrode largely retained its structural integrity. The separator shows only minimal coating material deposition. The residual electrolyte on the separator exhibits a pale yellow coloration, indicating decomposition and parasitic side reactions that occur during prolonged cycling at 100 °C. Cross-sectional SEM analysis of the cycled SiNQ@C-rGO

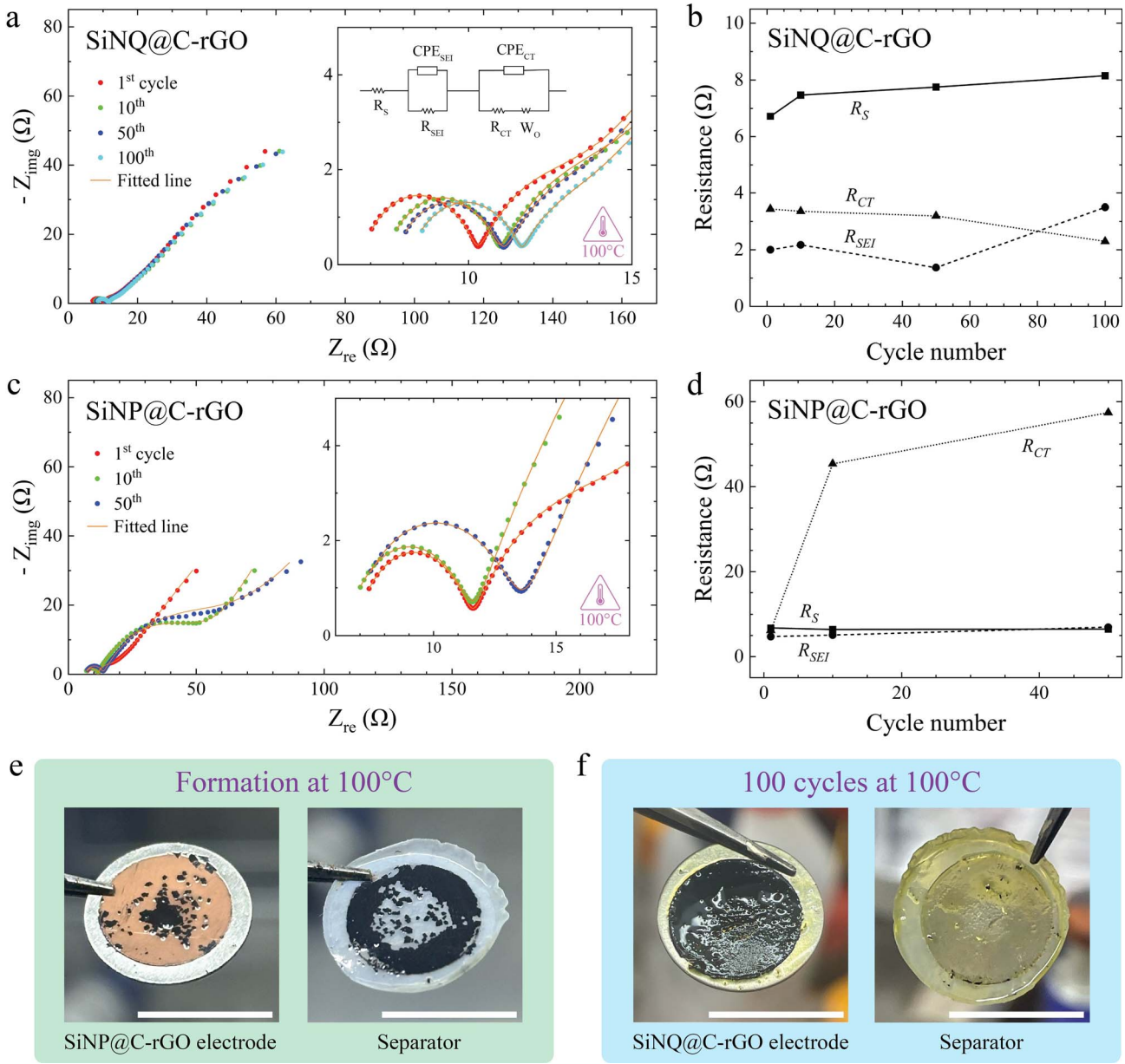

Fig. 4 (a and b) EIS results of the SiNQ@C-rGO cell, (c and d) EIS results of the SiNP@C-rGO cell, (e) digital images of the SiNP@C-rGO electrode and separator after the formation cycle at 100 °C, and (f) digital images of the SiNQ@C-rGO electrode and separator after 100 cycles at 100 °C. The scale bars in panels e and f represent a length of 12 mm.

electrode (Fig. S4) reveals pronounced electrode thickening from 31 μm (pristine) to 64 μm (cycled), indicative of substantial SEI growth and surface roughening. These observations confirm that although the SiNQ@C-rGO electrode demonstrates exceptional performance among Si-based electrodes under high-temperature (100 °C) conditions, SEI stability remains a critical challenge. Given that accelerated aging tests are often conducted at high temperatures, achieving high-capacity retention of ~73% over 100 cycles, despite elevated temperatures, high mass loading, and the use of a commercial polymeric separator, demonstrates the impressive thermal and electrochemical robustness of the SiNQ@C-rGO material design.

Conclusions

Novel SiNQs, characterized by a porous one-dimensional morphology and a unique structure comprising elemental Si pockets distributed within an amorphous Si suboxide matrix, were employed in this work as the active material for high-temperature battery anodes. The surface of SiNQ nanoparticles was modified using a dual-carbon protection strategy to form micron-sized SiNQ@C-rGO particles. The resulting SiNQ@C-rGO electrode combines several advantages desirable for high-temperature battery applications. These include (i) a relatively high SiNQ mass loading of 0.8–0.9 mg cm^{-2}, (ii) an industry-relevant electrode fabrication process based on an

aqueous slurry and copper foil current collector, (iii) robust cycling stability at 100 °C, with 73% capacity retention after 100 cycles at 420 mA g^{-1}, and (v) high rate capability, delivering ~1000 mA h g^{-1} (0.9 mA h cm^{-2}) at 840 mA g^{-1} at 100 °C. In comparison, the SiNP@C-rGO electrode (prepared using commercial solid SiNPs) exhibited poor cycling stability, rapid capacity decay, and premature electrode pulverization at 100 °C. Although coupled electrochemical and microstructural analyses indicate that further improvements could be achieved by enhancing the stability of the SEI layer, the SiNQ-based anodes show strong potential for advancing thermally resilient LIBs for next-generation lightweight hybrid and electric vehicles.

Author contributions

Janak Basel: data curation, formal analysis, methodology, software, visualization, writing – original draft. Morteza Sabet: conceptualization, funding acquisition, formal analysis, investigation, methodology, validation, visualization, writing – original draft. Peshal Karki: formal analysis, methodology, writing – review & editing. Mihir Parekh: investigation, methodology, formal analysis, validation, writing – original draft. Talia M. Sebastian: investigation, resources, validation, writing – review & editing. Yi Ding: investigation, resources, validation, writing – review & editing. Apparao M. Rao: conceptualization, funding acquisition, investigation, project administration, resources, supervision, validation, writing – review & editing.

Conflicts of interest

There are no conflicts to declare.

Data availability

The supporting data has been provided as part of the supplementary information (SI). Supplementary information: S-TEM images of SiNQ@C-rGO; SEM images of as-prepared electrodes; further analysis of the cycling performance of electrodes at 100 °C; (dis)charge capacity data; differential capacity curves for selected cycles; SEM image of the cycled SiNQ@C-rGO electrode; literature survey of the electrochemical performance of positive and negative electrodes at or above 100 °C; and surface area and pore volume of pristine SiNQs and SiNPs and their rGO composites. See DOI: https://doi.org/10.1039/d6ta00784h.

Acknowledgements

This work was supported by Clemson University's Virtual Prototyping of Autonomy Enabled Ground Systems (VIPR-GS) under Cooperative Agreement W56HZV-21-2-0001 with the US Army DEVCOM Ground Vehicle Systems Center (GVSC). All battery and Raman data presented herein were obtained at the Clemson Nanomaterials Institute, which is operated by Clemson University. The authors acknowledge Parsa Sabet, Charles Townes Center at Sterling School, for assistance with preparing the graphical abstract. DISTRIBUTION STATEMENT A. Approved for public release; distribution is unlimited. OPSEC10153.

References

1 A. S. Aricò, P. Bruce, B. Scrosati, J.-M. Tarascon, and W. V. Schalkwijk, *Nanostructured Materials for Advanced Energy Conversion and Storage Devices*, 2005, https://www.nature.com/naturematerials.
2 X. Lin, M. Salari, L. M. R. Arava, P. M. Ajayan and M. W. Grinstaff, High Temperature Electrical Energy Storage: Advances, Challenges, and Frontiers, *Chem. Soc. Rev.*, 2016, **7**, 5848–5887, DOI: 10.1039/c6cs00012f.
3 M. S. Whittingham, Lithium Batteries and Cathode Materials, *Chem. Rev.*, 2004, **104**(10), 4271–4301, DOI: 10.1021/cr020731c.
4 X. Xu, W. Li, B. Xu and J. Qin, Numerical Study on a Water Cooling System for Prismatic LiFePO4 Batteries at Abused Operating Conditions, *Appl. Energy*, 2019, **250**, 404–412, DOI: 10.1016/j.apenergy.2019.04.180.
5 A. Rao, B. Lu, M. Parekh and X. Morteza Sabet, Lithium-Ion Battery Fires Are a Growing Public Safety Concern — Here's How to Reduce the Risk, *The Conversation*, 2023, 209359.
6 M.-T. F. Rodrigues, G. Babu, H. Gullapalli, K. Kalaga, F. N. Sayed, K. Kato, J. Joyner and P. M. Ajayan, A Materials Perspective on Li-Ion Batteries at Extreme Temperatures, *Nat. Energy*, 2017, **2**(8), 17108, DOI: 10.1038/nenergy.2017.108.
7 B. Scrosati and J. Garche, Lithium Batteries: Status, Prospects and Future, *J. Power Sources*, 2010, 2419–2430, DOI: 10.1016/j.jpowsour.2009.11.048.
8 A. Chagnes, M. Diaw, B. Carré, P. Willmann and D. Lemordant, Imidazolium-Organic Solvent Mixtures as Electrolytes for Lithium Batteries, *J. Power Sources*, 2005, **145**(1), 82–88, DOI: 10.1016/j.jpowsour.2004.12.035.
9 J. Xu, J. Yang, Y. NuLi, J. Wang and Z. Zhang, Additive-Containing Ionic Liquid Electrolytes for Secondary Lithium Battery, *J. Power Sources*, 2006, **160**(1), 621–626, DOI: 10.1016/j.jpowsour.2006.01.054.
10 M. Wang, Z. Shan, J. Tian, K. Yang, X. Liu, H. Liu and K. Zhu, Mixtures of Unsaturated Imidazolium Based Ionic Liquid and Organic Carbonate as Electrolyte for Li-Ion Batteries, *Electrochim. Acta*, 2013, **95**, 301–307, DOI: 10.1016/j.electacta.2013.02.032.
11 J. Reiter and M. Nadherna, N.-Allyl-N-Methylpiperidiniumbis(Trifluoromethanesulfonyl)Imide - A Film Forming Ionic Liquid for Graphite Anode of Li-Ion Batteries, *Electrochim. Acta*, 2012, **71**, 22–26, DOI: 10.1016/j.electacta.2012.03.088.
12 X. Lin, R. Kavian, Y. Lu, Q. Hu, Y. Shao-Horn and M. W. Grinstaff, Thermally-Responsive, Nonflammable Phosphonium Ionic Liquid Electrolytes for Lithium Metal Batteries: Operating at 100 Degrees Celsius, *Chem. Sci.*, 2015, **6**(11), 6601–6606, DOI: 10.1039/c5sc01518a.
13 B. Scrosati, J. Hassoun and Y. K. Sun, Lithium-Ion Batteries. A Look into the Future, *Energy Environ. Sci.*, 2011, 3287–3295, DOI: 10.1039/c1ee01388b.

14 C. Arbizzani, G. Gabrielli and M. Mastragostino, Thermal Stability and Flammability of Electrolytes for Lithium-Ion Batteries, *J. Power Sources*, 2011, **196**(10), 4801–4805, DOI: 10.1016/j.jpowsour.2011.01.068.

15 T. Sato, T. Maruo, S. Marukane and K. Takagi, Ionic Liquids Containing Carbonate Solvent as Electrolytes for Lithium Ion Cells, *J. Power Sources*, 2004, **138**(1–2), 253–261, DOI: 10.1016/j.jpowsour.2004.06.027.

16 E. De Santis, A. Aurora, S. Bergamasco, A. Rinaldi, R. Araneo and G. Battista Appetecchi, Ionic Liquid Electrolyte Technologies for High-Temperature Lithium Battery Systems, *Int. J. Mol. Sci.*, 2025, **26**(7), 3430, DOI: 10.3390/ijms26073430.

17 M. J. Marczewski, B. Stanje, I. Hanzu, M. Wilkening and P. Johansson, "Ionic Liquids-in-Salt"- a Promising Electrolyte Concept for High-Temperature Lithium Batteries?, *Phys. Chem. Chem. Phys.*, 2014, **16**(24), 12341–12349, DOI: 10.1039/c4cp01133c.

18 H. Niu, L. Wang, P. Guan, N. Zhang, C. Yan, M. Ding, X. Guo, T. Huang and X. Hu, Recent Advances in Application of Ionic Liquids in Electrolyte of Lithium Ion Batteries, *J. Energy Storage*, 2021, **40**, 102659, DOI: 10.1016/j.est.2021.102659.

19 M. Galiński, A. Lewandowski and I. Stepniak, Ionic Liquids as Electrolytes, *Electrochim. Acta*, 2006, **15**, 5567–5580, DOI: 10.1016/j.electacta.2006.03.016.

20 N. Plylahan, M. Kerner, D. H. Lim, A. Matic and P. Johansson, Ionic Liquid and Hybrid Ionic Liquid/Organic Electrolytes for High Temperature Lithium-Ion Battery Application, *Electrochim. Acta*, 2016, **216**, 24–34, DOI: 10.1016/j.electacta.2016.08.025.

21 K. Ababtain, G. Babu, X. Lin, M. T. F. Rodrigues, H. Gullapalli, P. M. Ajayan, M. W. Grinstaff and L. M. R. Arava, Ionic Liquid-Organic Carbonate Electrolyte Blends to Stabilize Silicon Electrodes for Extending Lithium Ion Battery Operability to 100 °c, *ACS Appl. Mater. Interfaces*, 2016, **8**(24), 15242–15249, DOI: 10.1021/acsami.6b02620.

22 S. Rajendran, V. S. Ganesan and L. M. R. Arava, Electrochemical Instability of Room-Temperature Ionic Liquids with LiTFSI at Elevated Temperature and Its Consequences in Li/Li-Ion Based Half-Cells and Full-Cells, *Electrochim. Acta*, 2024, **498**, 144599, DOI: 10.1016/j.electacta.2024.144599.

23 A. Lewandowski and A. Świderska-Mocek, Ionic Liquids as Electrolytes for Li-Ion Batteries-An Overview of Electrochemical Studies, *J. Power Sources*, 2009, 601–609, DOI: 10.1016/j.jpowsour.2009.06.089.

24 V. Baranchugov, E. Markevich, E. Pollak, G. Salitra and D. Aurbach, Amorphous Silicon Thin Films as a High Capacity Anodes for Li-Ion Batteries in Ionic Liquid Electrolytes, *Electrochem. Commun.*, 2007, **9**(4), 796–800, DOI: 10.1016/j.elecom.2006.11.014.

25 K. Kim, Y. H. Cho and H. C. Shin, 1-Ethyl-1-Methyl Piperidinium Bis(Trifluoromethanesulfonyl)Imide as a Co-Solvent in Li-Ion Batteries, *J. Power Sources*, 2013, **225**, 113–118, DOI: 10.1016/j.jpowsour.2012.10.038.

26 H. Yang, G. V. Zhuang and P. N. Ross, Thermal Stability of LiPF6 Salt and Li-Ion Battery Electrolytes Containing LiPF6, *J. Power Sources*, 2006, **161**(1), 573–579, DOI: 10.1016/j.jpowsour.2006.03.058.

27 Z. Lu, L. Yang and Y. Guo, Thermal Behavior and Decomposition Kinetics of Six Electrolyte Salts by Thermal Analysis, *J. Power Sources*, 2006, **156**(2), 555–559, DOI: 10.1016/j.jpowsour.2005.05.085.

28 E. Zinigrad, L. Larush-Asraf, G. Salitra, M. Sprecher and D. Aurbach, On the Thermal Behavior of Li Bis(Oxalato) Borate LiBOB, *Thermochim. Acta*, 2007, **457**(1–2), 64–69, DOI: 10.1016/j.tca.2007.03.001.

29 G. B. Appetecchi, W. Henderson, and P. Villano, *The Surface Film Formed on a Lithium Metal Electrode in a New Imide Electrolyte, Lithium Bis(Perfluoroethylsulfonylimide) [LiN($C_2F_5SO_2$)$_2$] You May Also like PEO-LiN ($SO_2CF_2CF_3$)$_2$ Polymer Electrolytes: I. XRD, DSC, and Ionic Conductivity Characterization Poly(Ethylene Oxide) LiN ($SO_2CF_2CF_3$)$_2$ Polymer Electrolytes*, 1999.

30 M. Dahbi, F. Ghamouss, F. Tran-Van, D. Lemordant and M. Anouti, Comparative Study of EC/DMC LiTFSI and LiPF6 Electrolytes for Electrochemical Storage, *J. Power Sources*, 2011, **196**(22), 9743–9750, DOI: 10.1016/j.jpowsour.2011.07.071.

31 M. Dahbi, F. Ghamouss, F. Tran-Van, D. Lemordant and M. Anouti, Ester Based Electrolyte with Lithium Bis(Trifluoromethane Sulfonyl) Imide Salt for Electrochemical Storage Devices: Physicochemical and Electrochemical Characterization, *Electrochim. Acta*, 2012, **86**, 287–293, DOI: 10.1016/j.electacta.2012.02.080.

32 F. Mestre-Aizpurua, S. Hamelet, C. Masquelier and M. R. Palacín, High Temperature Electrochemical Performance of Nanosized LiFePO4, *J. Power Sources*, 2010, **195**(19), 6897–6901, DOI: 10.1016/j.jpowsour.2010.03.097.

33 W. Jiang, Z. Liu, Q. Kong, J. Yao, C. Zhang, P. Han and G. Cui, A High Temperature Operating Nanofibrous Polyimide Separator in Li-Ion Battery, *Solid State Ionics*, 2013, **232**, 44–48, DOI: 10.1016/j.ssi.2012.11.010.

34 F. Mestre-Aizpurua, S. Hamelet, C. Masquelier and M. R. Palacín, High Temperature Electrochemical Performance of Nanosized LiFePO4, *J. Power Sources*, 2010, **195**(19), 6897–6901, DOI: 10.1016/j.jpowsour.2010.03.097.

35 Y. Guo, B. Feng, Y. Wang, J. Zhao, C. Zhou, X. Wang, L. Yang, Z. Jin, Z. Hu and Q. Wu, A Thermally Managed Separator for Lithium Metal Batteries Operating Safely above 100 °C, *Nano Energy*, 2025, **133**, 110472, DOI: 10.1016/j.nanoen.2024.110472.

36 R. R. Kohlmeyer, G. A. Horrocks, A. J. Blake, Z. Yu, B. Maruyama, H. Huang and M. F. Durstock, Pushing the Thermal Limits of Li-Ion Batteries, *Nano Energy*, 2019, **64**, 103927, DOI: 10.1016/j.nanoen.2019.103927.

37 T. Chen, Z. Jin, Y. Liu, X. Zhang, H. Wu, M. Li, W. W. Feng, Q. Zhang and C. Wang, Stable High-Temperature Lithium-Metal Batteries Enabled by Strong Multiple Ion–Dipole Interactions, *Angew. Chem., Int. Ed.*, 2022, **61**(35), e202207645, DOI: 10.1002/anie.202207645.

38 X. Wu, T. Liu, Y. G. Lee and J. F. Whitacre, Glycerol Triacetate-Based Flame Retardant High-Temperature Electrolyte for the Lithium-Ion Battery, *ACS Appl. Mater. Interfaces*, 2024, **16**(19), 24590–24600, DOI: 10.1021/acsami.4c02323.

39 J. Wang, Q. Zheng, M. Fang, S. Ko, Y. Yamada and A. Yamada, Concentrated Electrolytes Widen the Operating Temperature Range of Lithium-Ion Batteries, *Advanced Science*, 2021, **8**(18), 2101646, DOI: 10.1002/advs.202101646.

40 L. Jiang, C. Liang, H. Li, Q. Wang and J. Sun, Safer Triethyl-Phosphate-Based Electrolyte Enables Nonflammable and High-Temperature Endurance for a Lithium Ion Battery, *ACS Appl. Energy Mater.*, 2020, **3**(2), 1719–1729, DOI: 10.1021/acsaem.9b02188.

41 S. Nagarajan, S. Hwang, C. Jaye, C. Weiland, D. M. Meira, M. Balasubramanian and L. M. R. Arava, Investigation of Electrode-Electrolyte Interfaces to Enable Non-Flammable Li-Ion Batteries Operating up to 125°C with Liquid Electrolyte, *Cell Rep. Phys. Sci.*, 2025, **6**(5), 102597, DOI: 10.1016/j.xcrp.2025.102597.

42 L. Yao, X. Wang, D. Li, X. Wang, H. Zhang, N. Wang, C. Shi and F. Ding, High-Concentrated Electrolyte Design Enables Lithium-Ion Pouch Batteries to Stably Operate at Extremely High Temperatures, *Electrochemistry*, 2024, **92**(5), 057004, DOI: 10.5796/electrochemistry.24-00031.

43 W. Jiang, Z. Liu, Q. Kong, J. Yao, C. Zhang, P. Han and G. Cui, A High Temperature Operating Nanofibrous Polyimide Separator in Li-Ion Battery, *Solid State Ionics*, 2013, **232**, 44–48, DOI: 10.1016/j.ssi.2012.11.010.

44 X. Wu, T. Liu, Y. G. Lee and J. F. Whitacre, Glycerol Triacetate-Based Flame Retardant High-Temperature Electrolyte for the Lithium-Ion Battery, *ACS Appl. Mater. Interfaces*, 2024, **16**(19), 24590–24600, DOI: 10.1021/acsami.4c02323.

45 X. Liu, L. Yin, D. Ren, L. Wang, Y. Ren, W. Xu, S. Lapidus, H. Wang, X. He, Z. Chen, G. L. Xu, M. Ouyang and K. Amine, In Situ Observation of Thermal-Driven Degradation and Safety Concerns of Lithiated Graphite Anode, *Nat. Commun.*, 2021, **12**(1), 4235, DOI: 10.1038/s41467-021-24404-1.

46 K. Kalaga, M. T. F. Rodrigues, H. Gullapalli, G. Babu, L. M. R. Arava and P. M. Ajayan, Quasi-Solid Electrolytes for High Temperature Lithium Ion Batteries, *ACS Appl. Mater. Interfaces*, 2015, **7**(46), 25777–25783, DOI: 10.1021/acsami.5b07636.

47 T. Zheng, J. Xiong, B. Zhu, X. Shi, Y. J. Cheng, H. Zhao and Y. Xia, From −20 °C to 150 °C: A Lithium Secondary Battery with a Wide Temperature Window Obtainedviamanipulated Competitive Decomposition in Electrolyte Solution, *J. Mater. Chem. A*, 2021, **9**(14), 9307–9318, DOI: 10.1039/d1ta00895a.

48 M. T. F. Rodrigues, K. Kalaga, H. Gullapalli, G. Babu, A. L. M. Reddy and P. M. Ajayan, Hexagonal Boron Nitride-Based Electrolyte Composite for Li-Ion Battery Operation from Room Temperature to 150 °C, *Adv. Energy Mater.*, 2016, **6**(12), 1600218, DOI: 10.1002/aenm.201600218.

49 P. K. Alaboina, Y. Ge, M. J. Uddin, Y. Liu, D. Lee, S. Park, X. Zhang and S. J. Cho, Nanoscale Porous Lithium Titanate Anode for Superior High Temperature Performance, *ACS Appl. Mater. Interfaces*, 2016, **8**(19), 12127–12133, DOI: 10.1021/acsami.6b00895.

50 K. A. Ababtain, *Design And Optimization Of Lithium Ion Battery For High Temperature Applications*, 2016, https://digitalcommons.wayne.edu/oa_dissertations/1613.

51 X. Zuo, J. Zhu, P. Müller-Buschbaum and Y. J. Cheng, Silicon Based Lithium-Ion Battery Anodes: A Chronicle Perspective Review, *Nano Energy*, 2017, 113–143, DOI: 10.1016/j.nanoen.2016.11.013.

52 M. Rana, A. Pendashteh, R. S. Schäufele, J. Gispert and J. J. Vilatela, Eliminating Solvents and Polymers in High-Performance Si Anodes by Gas-Phase Assembly of Nanowire Fabrics, *Adv. Energy Mater.*, 2022, **12**(26), 2103469, DOI: 10.1002/aenm.202103469.

53 P. Karki, M. Sabet, M. Parekh, N. Sapkota, S. Tewari, Y. Ding, S. Pilla and A. Rao, In Situ Reduction in Carbon Disorder during Electrochemical Cycling of Silicon-Carbon Composite Anodes, *ACS Appl. Mater. Interfaces*, 2025, **17**(33), 46909–46923, DOI: 10.1021/acsami.5c05917.

54 M. J. Piernas-Muñoz, S. E. Trask, A. R. Dunlop, E. Lee and I. Bloom, Effect of Temperature on Silicon-Based Anodes for Lithium-Ion Batteries, *J. Power Sources*, 2019, **441**, 227080, DOI: 10.1016/j.jpowsour.2019.227080.

55 E. Zhao, S. Luo, Y. Gu, L. Yang and S. Hirano, Preactivation Strategy for a Wide Temperature Range *In Situ* Gel Electrolyte-Based LiNi 0.5 Co 0.2 Mn 0.3 O 2 ‖Si–Graphite Battery, *ACS Appl. Mater. Interfaces*, 2021, **13**(50), 59843–59854, DOI: 10.1021/acsami.1c15888.

56 Y. Ha, D. P. Finegan, A. M. Colclasure, S. E. Trask and M. Keyser, Evaluating Temperature Dependent Degradation Mechanisms of Silicon-Graphite Electrodes and the Effect of Fluoroethylene Carbonate Electrolyte Additive, *Electrochim. Acta*, 2021, **394**, 139097, DOI: 10.1016/j.electacta.2021.139097.

57 Q. Xia, A. Xu, L. Du, Y. Yan and S. Wu, High-Rate, Long-Term Performance of LTO-Pillared Silicon/Carbon Composites for Lithium-Ion Batteries Anode under High Temperature, *J. Alloys Compd.*, 2019, **800**, 50–57, DOI: 10.1016/j.jallcom.2019.06.023.

58 L. Fu, A. Xu, Y. Song, J. Ju, H. Sun, Y. Yan and S. Wu, Pinecone-like Silicon@Carbon Microspheres Covered by Al2O3 Nano-Petals for Lithium-Ion Battery Anode under High Temperature, *Electrochim. Acta*, 2021, **387**, 138461, DOI: 10.1016/j.electacta.2021.138461.

59 N. Chen, M. Sabet, N. Sapkota, M. Parekh, S. Chiluwal, K. Koehler, C. M. Clemons, Y. Ding, A. M. Rao and S. Pilla, Bioderived Silicon Nano-Quills: Synthesis, Structure and Performance in Lithium-Ion Battery Anodes, *Green Chem.*, 2024, **26**(8), 4691–4702, DOI: 10.1039/d4gc00498a.

60 N. Sapkota, M. Sabet, N. Chen, M. Parekh, J. Basel, Y. Ding and A. Rao, Multifunctional Dual Carbon Framework for Self-Healing Silicon Anodes, *ACS Appl. Mater. Interfaces*, 2025, **17**(37), 52077–52089, DOI: 10.1021/acsami.5c11083.

61 T. Dash, B. Bihari Palei, B. Dash, R. Kumar Sahu, R. Kumar Moharana, S. Dhar and S. Kumar Biswal, Graphene Reinforced Silicon Composites and Their Characterizations, *Mater. Today Proc.*, 2022, **62**, 5962–5964, DOI: 10.1016/j.matpr.2022.04.721.

62 C. Meier, S. Lüttjohann, V. G. Kravets, H. Nienhaus, A. Lorke and H. Wiggers, Raman Properties of Silicon Nanoparticles, *Phys. E*, 2006, **32**(1–2), 155–158, DOI: 10.1016/j.physe.2005.12.030.

63 K. Feng, W. Ahn, G. Lui, H. Woong Park, A. Ghorbani Kashkooli, G. Jiang, X. Wang, X. Xiao, and Z. Chen, *Implementing an In-Situ Carbon Network in Si/Reduced Graphene Oxide for High Performance Lithium-Ion Battery Anodes*, 2015, https://www.sciencedirect.com/science/article/pii/S2211285515004048.

64 J. Chang, X. Huang, G. Zhou, S. Cui, P. B. Hallac, J. Jiang, P. T. Hurley and J. Chen, Multilayered Si Nanoparticle/Reduced Graphene Oxide Hybrid as a High-Performance Lithium-Ion Battery Anode, *Adv. Mater.*, 2014, **26**(5), 758–764, DOI: 10.1002/adma.201302757.

65 D. T. Rogstad, M.-A. Einarsrud and A. M. Svensson, High-Temperature Performance of Selected Ionic Liquids as Electrolytes for Silicon Anodes in Li-Ion Batteries, *J. Electrochem. Soc.*, 2022, **169**(11), 110531, DOI: 10.1149/1945-7111/ac9f78.

66 T. Tan, P.-K. Lee and D. Y. W. Yu, Improving Thermal Stability of Si-Based Anodes for Lithium-Ion Batteries by Controlling Bulk and Surface Layer Compositions, *J. Electrochem. Soc.*, 2021, **168**(10), 100527, DOI: 10.1149/1945-7111/ac2f07.

67 Z. Li, C. Stetson, S. Frisco, S. Harvey, Z. Huey, G. Teeter, C. Engtrakul, A. Burrell, X. Li and A. Zakutayev, The Role of Oxygen in Lithiation and Solid Electrolyte Interphase Formation Processes in Silicon-Based Anodes, *J. Electrochem. Soc.*, 2022, **169**(12), 120512, DOI: 10.1149/1945-7111/aca833.

68 J. Wu, Q. Dong, Q. Zhang, Y. Xu, X. Zeng, Y. Yuan and J. Lu, Fundamental Understanding of the Low Initial Coulombic Efficiency in SiOx Anode for Lithium-Ion Batteries: Mechanisms and Solutions, *Adv. Mater.*, 2024, **36**(33), 2405751, DOI: 10.1002/adma.202405751.

